Published Journal of Applied Physics, DOI: 10.1063/5.0314819, online on 11 Feb 2026, Vol.139, No. 6, 064101, 14 February 2026.

Machine learning and first-principles guided design of $BaTiO_3$-based materials for capacitor applications

Chong Guo[a,1], Kailing Fang[a,1], Haojie Yue [a], Kun Guo[a,*], Ziliang Deng[a], Zhichao Gong[a], Kang Li[a], Huacheng Zhang[a], Zhiyong Liu[a], Bing Xie[a], Pu Mao[a], Chee Kiang Ivan Tan[b], Kui Yao[b], Francis Eng Hock Tay[c]

[a] School of Power and Energy, Nanchang Hangkong University, Nanchang 330063, China

[b] Institute of Materials Research and Engineering (IMRE), A*STAR (Agency for Science, Technology and Research), 2 Fusionopolis Way, Innovis, 138634, Singapore

[c] Department of Mechanical Engineering, National University of Singapore, 9 Engineering Drive 1, Singapore 117575, Singapore

[*] Corresponding author at School of Power and Energy, Nanchang Hangkong University, Nanchang 330063, China.

[1] These authors contributed equally to this work.

E-mail address: guokun@nchu.edu.cn (K. Guo).

Abstract

Addressing the requirements of advanced capacitor applications for high dielectric permittivity, low loss, and strong frequency stability necessitates the accelerated development of materials exhibiting weakly coupled relaxor ferroelectric characteristics and broad temperature stability. $BaTiO_3$ systems have attracted considerable interest owing to their high dielectric constant and tunable properties. However, conventional trial-and-error approaches and complex doping strategies hinder rapid progress. In this study, a data-driven approach combining first-principles calculations with machine learning (ML) was employed to predict the variation trends in formation energies for 30,301 Sr, La co-doped $BaTiO_3$ compositions. The ferroelectric properties, crystal structures, elastic anisotropy, and thermal properties were systematically investigated at four representative doping levels (0, 0.125, 0.25, and 0.375) to elucidate the microscopic mechanism responsible for the emergence of weakly coupled relaxor ferroelectric behavior and to enable rapid identification of doping ranges that yield both relaxor ferroelectric characteristics and broad temperature stability. The results show that Sr, La co-doping in the range of 0.125–0.25 introduces compositional and displacement disorder that progressively suppresses long-range ferroelectric order, promotes the formation of polar nanoregions (PNRs), and drives the system toward a weakly coupled, relaxor-like dielectric response with reduced hysteretic loss, with the composition at 0.25 exhibiting enhanced mechanical and thermodynamic performance. These findings provide guidance for $BaTiO_3$-based materials for high-frequency capacitor applications and offer a transferable framework for accelerating the study of doped material properties.

Keywords: $BaTiO_3$ system, Machine learning, First-principles calculations, Relaxor ferroelectrics

Journal of Applied Physics

AIP Publishing

1. Introduction

The rapid advancement of artificial intelligence, the Internet of Things, 5G, smart vehicles, and other emerging technologies generates massive daily data transmission and processing demands. High-frequency capacitors, critical for high-speed data processing, signal transmission, and power management, are integral to supporting these technological developments. Among the various material systems employed in capacitor production, $BaTiO_3$ has emerged as a promising lead-free sustainable dielectric material due to its high dielectric constant, excellent ferroelectric properties, and low cost.[1,2] However, $BaTiO_3$ faces significant limitations in capacitor applications due to high energy loss form polarization hysteresis caused by strong ferroelectricity and dielectric anomalies near the Curie temperature arising from ferroelectric-paraelectric phase transitions. Therefore, modifying $BaTiO_3$ materials by introducing ion doping to identify ionic doping compositions possessing relaxor ferroelectric characteristics and broad temperature stability has become increasingly critical. The increasing complexity of materials research has rendered traditional trial-and-error approaches both time-consuming and cost-intensive, significantly slowing progress in the field.[3,4] Although first-principles calculations based on density functional theory (DFT) have advanced materials exploration by enabling detailed analysis of atomic and molecular structures, their efficiency is constrained by the vast chemical space and the inherent complexity of materials.[5]

Advances in artificial intelligence (AI) and big data have revolutionized materials science, enabling accelerated progress through efficient computational platforms and open-source materials databases.[6,7] In particular, machine learning (ML) techniques have emerged as powerful tools for predicting and screening unknown material systems. Recent progress includes predicting d_{33} values of new materials based on their features,[8] identifying perovskite materials for photovoltaic applications,[9] and forecasting material phase diagrams.[10] ML applications in materials science not only enhance research efficiency and reduce computational complexity but also reveal potential physical laws by analyzing the relationships between structures and compositions in material databases. Despite these advancements, research focused on using ML for doping modifications of specific material systems remains limited compared to studies on performance predictions for unknown materials in databases. The scarcity of doping-related data in open-source databases further constrains progress in this area, underscoring the untapped potential of ML in guiding material doping and modification studies.

Addressing the aforementioned challenges, we propose a data-driven approach of ML-assisted first-principles calculations to identify dielectric materials with relaxor ferroelectric characteristics and broad temperature stability, in which representative doping compositions are selected based on predicted formation energy trends that reflect the intrinsic stability of the doped configurations, as illustrated in Fig. 1. This study obtained data on 231 compositions of Sr and La co-doped $BaTiO_3$ systems through first-principles calculations. Subsequently, feature engineering was employed to meticulously select 82 significant input features, which served as the initial dataset for training and evaluating six classical ML models. The importance of these features

was analyzed using Shapley Additive Explanations (SHAP) methods. Next, the accuracy of the best-performing Extreme Gradient Boosting (XGBoost) and Multilayer Perceptron (MLP) predictive models was validated through first-principles calculations, and the best-performing XGBoost model was utilized to predict the formation energies of all 30,301 compositions. Finally, representative doping compositions were selected based on the distribution of formation energies predicted by the optimal ML model, and their ferroelectric properties, crystal structure, elastic anisotropy, and thermal properties were investigated using first-principles calculations to reveal the microscopic mechanisms governing phase transitions and relaxor behavior in the doped materials. The results indicated that at doping concentrations of 0.125-0.25, the material transitions from a saturated ferroelectric phase to a weakly coupled relaxor phase, with significant reduction in remnant polarization and coercive field accompanied by improved high-frequency response, mechanical stability, and thermal stability. Not only does this overcome the limitations of $BaTiO_3$ in capacitor applications, but it also greatly reduces research costs and development cycles, minimizes unnecessary computational resource consumption, and provides practical guidance for designing advanced capacitor materials with both high-frequency response characteristics and stability.

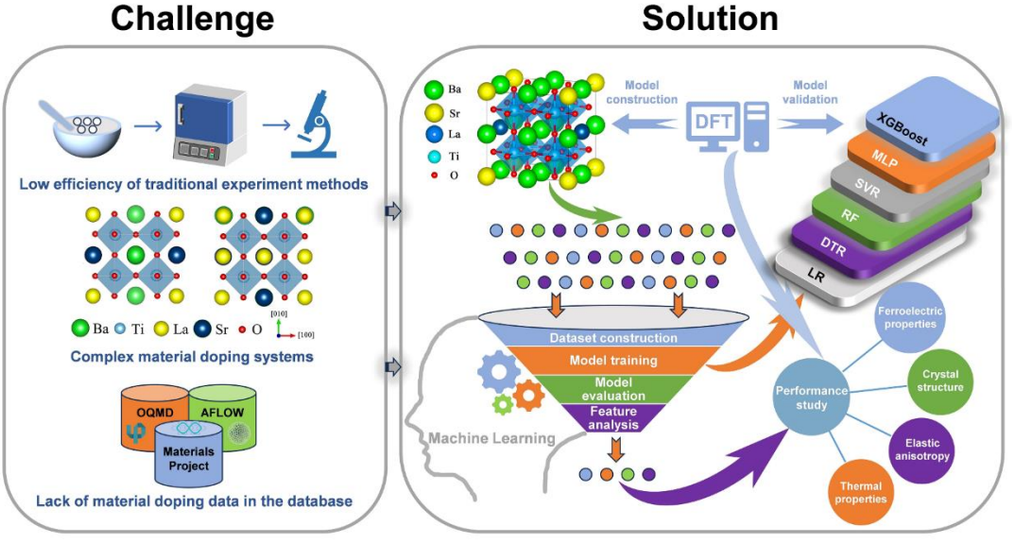

Fig. 1. Schematic diagram of A data-driven approach that integrates machine learning with first-principles calculations to accelerate the performance study of doped materials.

2. Methodology

Our approach consists of three main steps: (1) training and evaluating the best-performing ML models, followed by validation of their accuracy through first-principles calculations; (2) utilizing the best-performing ML models to predict the formation energy of all chemical compositions; (3) selecting representative doping compositions based on the distribution of formation energies predicted by the best-performing ML models and investigating their ferroelectric properties, crystal structure, elastic anisotropy, and thermal properties using first-principles calculations.

2.1 Machine learning algorithms

Enhancing the accuracy of predicting the formation energy of doped $BaTiO_3$ materials, we selected six ML algorithms from the open-source scikit-learn package:[11] Least Absolute Shrinkage and Selection Operator (LASSO),[12,13] Support Vector Regression (SVR),[14] Multilayer Perceptron (MLP),[15] Decision Tree Regression (DTR),[16] Random Forest (RF),[17] and Extreme Gradient Boosting (XGBoost).[18] These algorithms were chosen for their demonstrated performance in previous studies on general models for predicting formation energy and screening stable perovskite materials for solar cells.[19] The LASSO algorithm facilitates the rapid establishment of a baseline model, enabling convenient comparison with more complex models. The SVR algorithm effectively addresses nonlinear relationships through kernel functions, such as the RBF kernel. The MLP algorithm captures complex nonlinear relationships using multilayer neural networks. The DTR algorithm produces easily interpretable and visualizable decision tree models. The RF algorithm enhances model accuracy and robustness by integrating multiple decision trees, while the XGBoost algorithm exhibits exceptional predictive performance and generalization ability across a variety of applications.

2.2 Selection of doping elements and doping amounts in BT doping systems

The selection of doping elements and doping amounts in the $BaTiO_3$ (BT) system is critical to this study. Recent studies have demonstrated that doping Sr in the $BaTiO_3$ system reduces dielectric loss,[20,21] while La doping enhances the material's dielectric constant,[22,23] both aligning with the need for dielectric materials with rapid response capabilities. Although elements such as Mn, Zr, Gd, and Eu have shown similar effects,[24-26] Sr and La doping offer distinct advantages in optimizing the dielectric properties of $BaTiO_3$, particularly in regulating the Curie temperature, maintaining dielectric stability at high temperatures, and suppressing dielectric loss. Previous studies have demonstrated that material stability-related parameters, particularly phase energy differences and defect formation energies, exhibit significant correlations with the stability of doped systems, defect formation propensity, and electronic structure characteristics. These fundamental parameters can consequently provide critical guidance for determining optimal doping concentrations in material engineering applications.[27,28] We also observed that lower formation energy facilitates the incorporation of dopant elements into the lattice, altering the material's electronic structure and energy level distribution.[29] Furthermore, since the doping ratio of Sr and La is a key feature for predicting formation energy and further investigating ferroelectric properties, we focused on $BaTiO_3$ co-doped with equal amounts of Sr and La.[30] This approach enables a more accurate reflection of the individual effects of Sr and La doping on formation energy while facilitating a comparison of their relative impacts.

2.3 First-principles calculations

In this study, we constructed computational models with the formula $(Ba_{1-x-y}Sr_xLa_y)TiO_3$ (x = y = 0, 0.125, 0.25, and 0.375). The formation energy calculation

model for the $(Ba_{1-x-y}Sr_xLa_y)TiO_3$ system is derived from the calculation model in the ISCD file. For doped systems lacking a corresponding model in the ISCD library, we will utilize VESTA software to construct the model.[31] After the construction of the crystal structure model was completed, the formation energy data of these doped systems were calculated using the virtual crystal approximation (VCA) method in Materials Studio software. VCA is utilized as an alternative method for supercell construction, applicable to the calculation of doped system properties. Its principle is based on the mixing of individual atomic pseudopotentials to generate a virtual pseudopotential as $V_{VCA}^{ps}[x] = xV_{solute}^{ps} + (1-x)V_{solvent}^{ps}$.[32,33] After predicting the effects of Sr and La doping variations on the distribution of formation energy values using ML methods, we utilized VESTA software to model the crystal structures of pure $BaTiO_3$ and various doping levels of Sr and La. Crystal Structure models of $(Ba_{1-x-y}Sr_xLa_y)TiO_3$ were established with the *P4mm* space group. First-principles calculations were conducted within the density functional theory (DFT) framework using the Vienna Ab-initio Simulation Package (VASP).[34] Pseudopotentials were generated based on the following electronic configurations: Ba($5s^25p^66s^2$), Ti($3s^23p^64s^23d^2$), Sr($4s^24p^65s^2$), La($5s^25p^65d^16s^2$), and O($2s^22p^4$).[35-37] The energy convergence criterion was set to 1×10^{-6} eV/atom, and atomic positions and lattice parameters were relaxed until the forces on each atom converged to less than 0.001 eV/Å. Hubbard U corrections were applied to address strong electron-electron interactions in the localized Ti 3d and La 5d orbitals, with U values set to 4 eV and 6 eV, respectively.[38-40] Sr and La atoms substituted Ba at the A-sites of a 40-atom supercell to create structures with varying doping levels. The construction of these crystal structure models facilitates the subsequent validation of the ML formation energy prediction model and the investigation of the impact of different Sr and La doping levels on ferroelectric properties, crystal structure, elastic anisotropy, and thermal properties. It should be noted that in the present first-principles calculations, no explicit charge-compensation defects (e.g., Ti vacancies or O vacancies) were introduced. For the formation energy calculations, the charge balance was maintained through the VCA method, which inherently averages the pseudopotentials of Sr and La on the A-site to construct a "mixed pseudopotential." In this approach, the system achieves automatic charge averaging without explicitly introducing vacancies or excess charges, and thus remains charge neutral through the mixed potential itself. For the supercell-based calculations performed using VASP, the charge balance was maintained according to VASP's default electron-counting scheme, in which the total number of electrons is consistent with the valence electron count of all pseudopotentials. Any extra electrons introduced by the substitution of Ba^{2+} with La^{3+} are automatically included in the total electron number, and the code compensates the overall charge through a uniform background charge to ensure numerical convergence. This treatment effectively corresponds to an electronic compensation mechanism rather than ionic (vacancy-type) compensation. While the actual charge-compensation mechanism in experiments may involve Ti or O vacancies depending on synthesis conditions, the present work focuses on exploring compositional trends and intrinsic property evolution from a theoretical perspective.

3. Results and discussion

3.1 Dataset construction and feature engineering

Due to the lack of formation energy data for Sr and La co-doped $BaTiO_3$ systems in various open-source materials databases, and considering that the data in such databases are typically derived from first-principles calculations, we employed the VCA method in the Materials Studio simulation software to calculate the formation energy data for these doped systems. Given that the ionic radii of Sr and La closely resemble that of Ba, facilitating their occupancy of the A site in co-doped $BaTiO_3$, the chemical composition was formulated as $(Ba_{1-x-y}Sr_xLa_y)TiO_3$ (as illustrated in Fig. 2a). In subsequent studies of material doping, the condition x = y ensures equal amounts of Sr and La co-doped into the $BaTiO_3$.Changes in x and y yield different material compositions. To expedite the dataset construction, we selected chemical compositions with $\Delta x = 0.05$ and $\Delta y = 0.025$ from a total of 30,301 possible compositions（see details in Supplementary Dataset S1）. Doped structures for these compositions were constructed using the tetragonal perovskite structure of $BaTiO_3$ as the starting point. Ultimately, 231 compositions successfully formed crystal structures, and their formation energies were calculated. These compositions, along with their corresponding formation energy data, were compiled into the initial dataset for training our machine learning model（see details in Supplementary Dataset S2）.

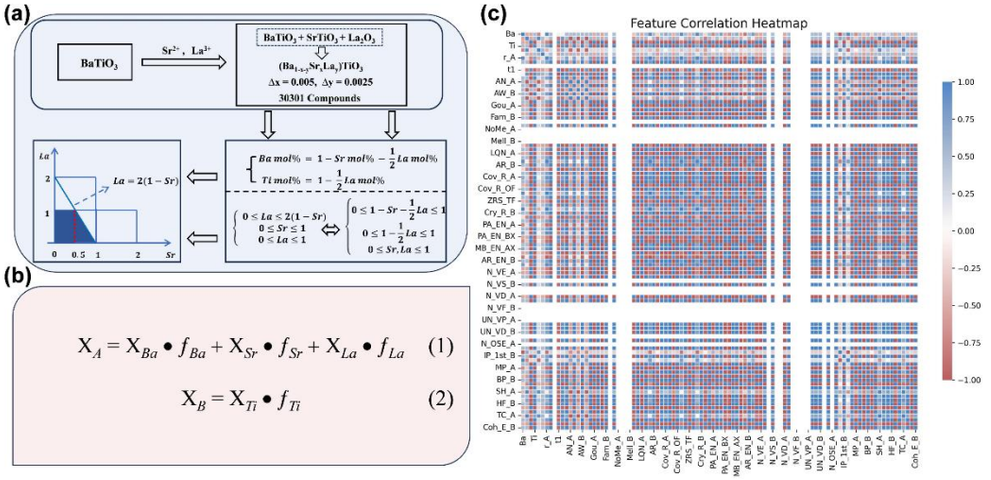

Fig. 2. (a) Sr^{2+} and La^{3+} co-doped $BaTiO_3$ system, illustrating the chemical composition, the relationship between the content of each element and the associated constraints, and the spatial distribution of the dopants within the system. (b) Feature construction: Development of A-site and B-site features for ABX_3 formulas under doping conditions using the weighted average method. (c) Feature selection: Pearson correlation coefficient heatmap.

Before training the formation energy prediction model, the initial step involves feature construction. Previous studies on ABX_3-type perovskite materials generated features by distinguishing the attributes of elements occupying the A, B, and X sites.[41] However, this approach is not applicable to our study, as the chemical composition of the initial dataset for the Sr, La co-doped $BaTiO_3$ system comprises five different types of elements. Drawing inspiration from the concept that dopant elements with similar ionic radii can enter crystal structures, we developed new features using a weighted

average method, as illustrated in Fig. 2b. The A-site features were calculated as the sum of the products of the features of each occupying element and their respective molar fractions. The B-site, occupied solely by Ti, has its feature defined as the product of Ti's feature and its molar fraction, reflecting the changes in content due to doping. Since the X-site is consistently occupied by O and remains unchanged, no features were generated for this site in this study. After preliminary screening, an initial set of 100 features was obtained. Abbreviations for full-text features and other abbreviations are in Table S1.

Subsequently, the Pearson correlation coefficients for the 100 feature columns were calculated, and a partial heatmap of the features was generated, as shown in Fig. 2c (The full heatmap is in Supplementary Fig. S1). The results revealed that most A-site features and B-site features constructed using formulas (1) and (2) in Fig. 2b exhibited high Pearson correlation coefficients, which are commonly indicative of strong linear associations between features and pose potential risk of multicollinearity issues. This correlation is typically attributed to the shared information among features, particularly when employing the weighted averaging method, which tends to produce overly similar elemental characteristics across different chemical compositions, thereby inducing collinearity issues. Furthermore, the limited variation in molar amounts of elements within the doping system would also exacerbate such correlations. Previous studies utilizing similar feature engineering methods for optimizing doped material properties have likewise encountered these high inter-feature correlation.[8] To address this issue, non-linear models, such as XGBoost, Random Forest and Gradient Boosting Decision Trees, were prioritized during model training. These models are less affected by multicollinearity and can effectively manage feature redundancy through node splitting. Through comprehensive analysis of the complete Pearson correlation coefficient heatmap across 100 feature columns (as illustrated in Supplementary Fig. S1), it was observed that 16 columns exhibited constant-valued characteristics. These invariant features were identified as potential contributors to computational redundancy and were consequently removed to mitigate their adverse effects on model generalization capability. Additionally, one descriptive feature not involved in model training and one target feature were systematically excluded during the formal model training phase to prevent information leakage. This rigorous feature selection process resulted in the retention of 82 optimal input features, ultimately yielding an initial dataset comprising 231 rows and 82 columns. (see details in Supplementary Dataset S3).

3.2 Model training and performance evaluation

The initial dataset was divided into training and test sets in a 4:1 ratio. Six regression algorithms, including Linear Regression (LR), Support Vector Regression (SVR), Multilayer Perceptron (MLP), Decision Tree Regression (DTR), Random Forest (RF), and Extreme Gradient Boosting (XGBoost), were employed to predict the formation energy of the materials (Algorithm details and parameter settings are in Table S2). The results are illustrated in Fig. 3. Panels (a) through (f) of Fig. 3 compare the expected formation energy values with those obtained from first-principles calculations

for each algorithm. In these figures, blue points represent data from the training set, while green points denote data from the test set. The horizontal axis indicates the formation energy values derived from first-principles calculations, and the vertical axis displays the predicted formation energy values from each algorithm. A closer alignment of predicted values with actual values signifies higher prediction accuracy. The graphs demonstrate that the proximity of the test data points to the regression line (the red dashed line in the figures) reflects the model's generalization capability, thereby indicating the accuracy of its predictions for the formation energy of unknown compositions.

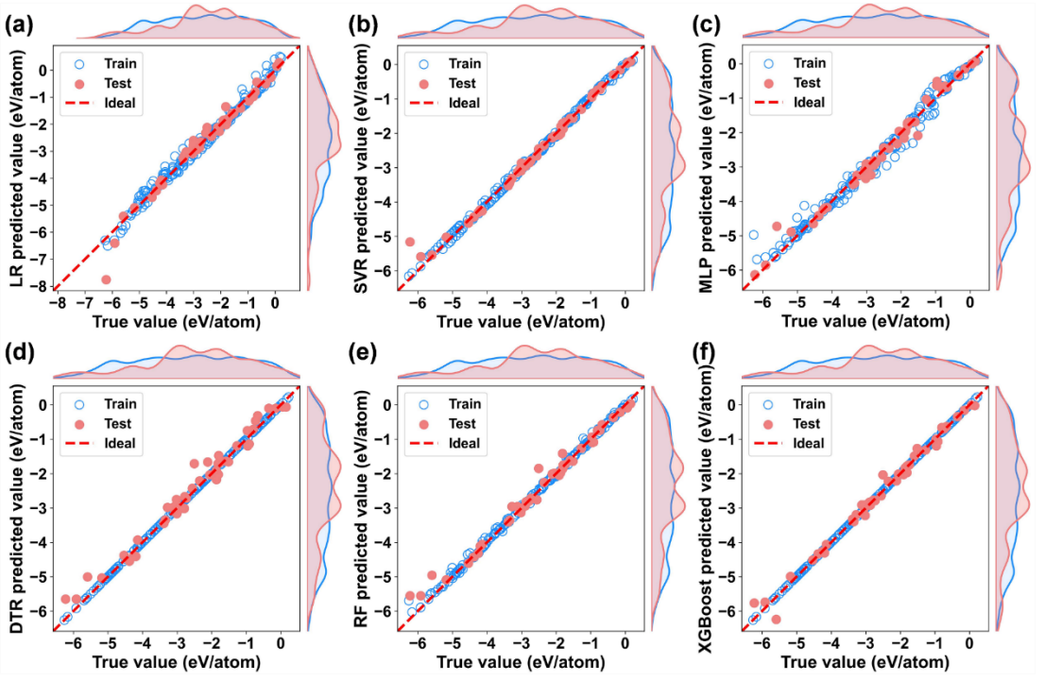

Fig. 3. Comparison of the actual formation energy and the predicted values from each model: (a) Linear Regression (LR); (b) Support Vector Regression (SVR); (c) Multilayer Perceptron (MLP); (d) Decision Tree Regression (DTR); (e) Random Forest (RF); (f) XGBoost.

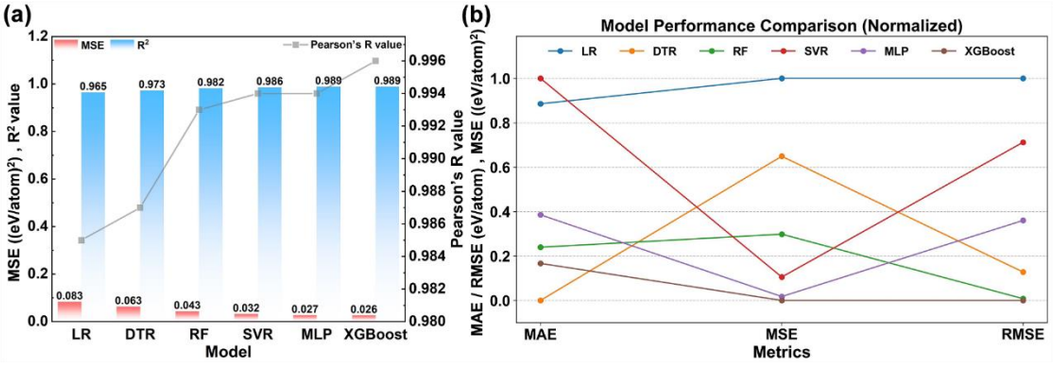

Fig. 4. (a) Performance comparison of six machine learning prediction models. (b) Normalized line plot comparison of error metrics (MAE, MSE, and RMSE) across six machine learning prediction models.

The predicted results are summarized in Table S3. From the data in Table S3 and Fig. 4(a) and (b), which reflect the performance ranking of the six ML prediction models, it is evident that the coefficient of determination (R^2) values are all greater than 0.96, demonstrating good training performance for each algorithm. Based on these results, the algorithms are ranked as follows: XGBoost, MLP, SVR, RF, DTR, and LR. In this study, the XGBoost model exhibited the best performance, with an R^2 of 0.989, a root mean square error (RMSE) of 0.162 eV/atom, and a mean absolute error (MAE) of 0.105 eV/atom. This demonstrates its reliable accuracy for formation energies in Sr and La co-doped $BaTiO_3$ systems, thereby supporting subsequent investigations into the overall trend of formation energy variations with doping concentrations.

3.3 Data prediction and feature analysis

The six formation energy prediction models developed in this study achieved the expected performance. These models were subsequently applied to predict the formation energy distribution across 30,301 compositions within the Sr and La co-doped $BaTiO_3$ system's chemical space, as shown in Fig. 5. In each subplot of Fig. 5, the shape of the formation energy distribution region forms a right-angled trapezoid, consistent with the shaded area depicted in Fig. 2a, which corresponds to the chemical space of the Sr and La co-doped $BaTiO_3$ system. Notably, the formation energy in all subplots predominantly resides in the negative region, indicating that most compounds within this system are to form. Furthermore, the formation energy distribution patterns across all subplots are highly similar, generally presenting a ring-like configuration. The region exhibiting the highest formation energy, represented by the reddest color, is situated near the center of the horizontal axis. Moving outward from this central region, the formation energy gradually decreases, with the lowest values found at the edges, corresponding to simpler chemical compositions. Analysis of the trends in Fig. 5 shows significant fluctuations in formation energy with increasing Sr content. In regions with high Sr content and elevated formation energy, increasing La content effectively reduces the formation energy. Moreover, the trends indicate that Sr content exerts a more pronounced influence on the system's formation energy than La content.

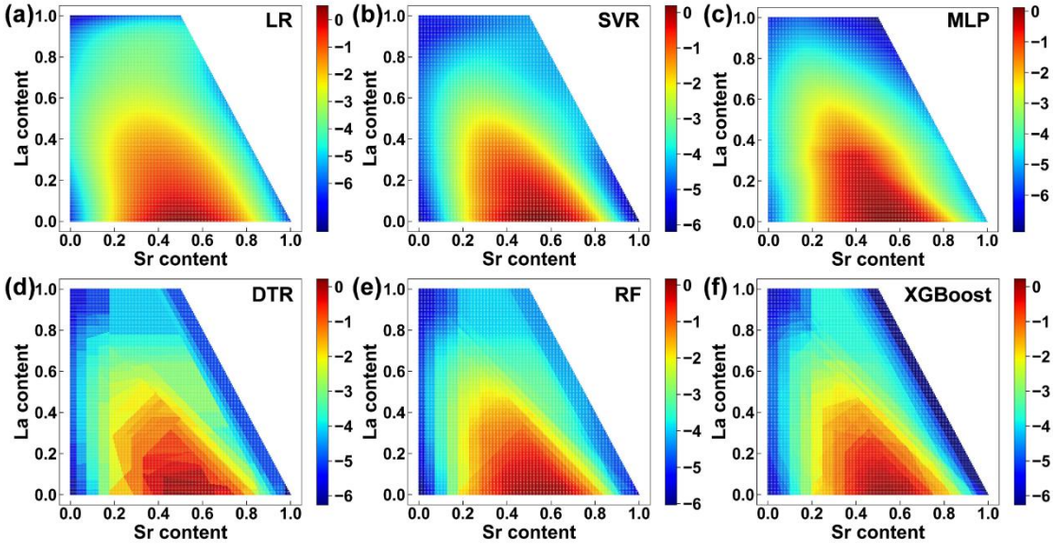

Fig. 5. Distribution of the predicted values for six different machine learning models in the Sr^{2+} and La^{3+} co-doped $BaTiO_3$ systems: (a) Linear Regression (LR); (b) Support Vector Regression (SVR); (c) Multilayer Perceptron (MLP); (d) Decision Tree Regression (DTR); (e) Random Forest (RF); (f) XGBoost.

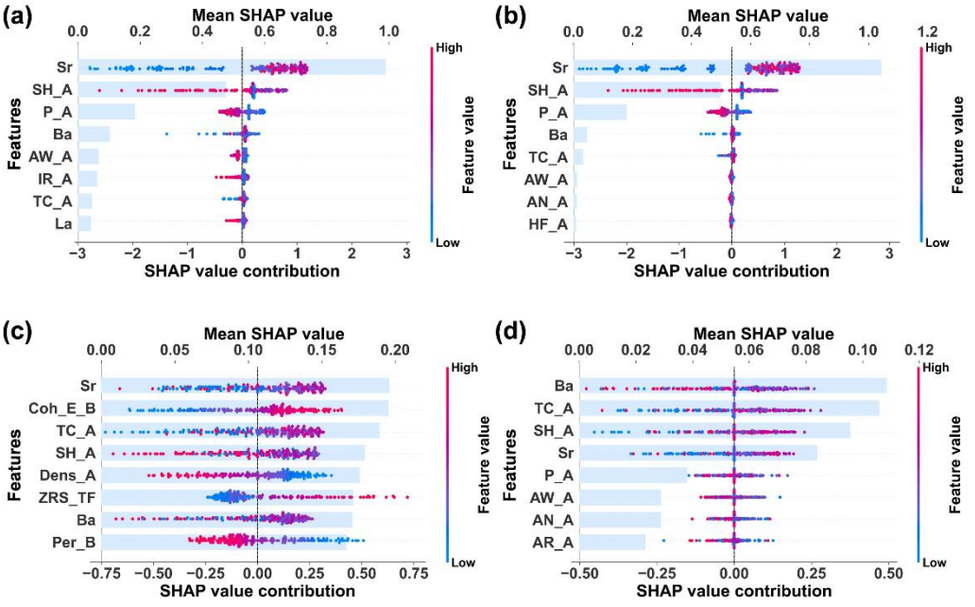

Fig. 6. Feature importance ranking and analysis based on SHAP interpretation: (a) XGBoost model; (b) Random Forest (RF) model; (c) Multilayer Perceptron (MLP) model; (d) Support Vector Regression (SVR) model.

The SHAP analysis was applied to interpret the top four formation energy prediction models (XGBoost, RF, MLP, and SVR), identifying the eight most influential features for each model (Fig. 6). For tree-based models (XGBoost and RF), we employed the TreeExplainer algorithm from the SHAP framework,[42] which efficiently calculates exact Shapley values by leveraging tree structure dependencies. In contrast, the KernelExplainer method was used for non-tree-based models (MLP and SVR),[43] approximating Shapley values through a kernel-weighted sampling approach. Due to the inherent differences in algorithm principles and underlying logic, the feature importance rankings varied among the models. A comparison of Fig. 6(a) and (b) reveals that the top eight features are nearly identical, with the top four being the same. However, slight differences exist in the distribution of these top features, although their correlation with the target property remains consistent. Specifically, the top four features, including Sr, specific heat capacity at the A-site (SH_A), polarizability at the A-site (P_A), and Ba, exhibit distinct correlations with the target property: positive (Sr, SH_A, Ba) and negative (P_A). From a physical standpoint, A-site-related thermodynamic and electronic descriptors are closely linked to lattice dynamics and bonding flexibility, as A-site substitution directly affects local strain, vibrational behavior, and electrostatic interactions in the perovskite lattice. The negative contribution of P_A suggests that enhanced A-site polarizability can partially screen electrostatic perturbations induced by doping, thereby stabilizing the structure, whereas

the positive correlations of Sr and SH_A reflect the increased energetic cost associated with lattice distortion upon substitution. Other features in the top eight also pertain to A-site characteristics, consistent with the fact that Sr and La co-dopants predominantly occupy the A-site in the $BaTiO_3$ system. Significant differences are observed when comparing Fig. 6(c) and (d): a B-site-related feature appears among the top eight contributors in the MLP model, whereas all top eight features in the SVR model are A-site-related, many of which overlap with those identified by the XGBoost and RF models. Notably, the features Ba, Sr, thermal conductivity at the A-site (TC_A), and SH_A consistently appear among the top contributors across all models, highlighting the dominant role of A-site-related lattice and bonding characteristics in governing the formation energy of the doped system.

3.4 Validation of the ML model with DFT

Further validating the accuracy of the formation energy prediction models developed in this study, crystal structure models of $BaTiO_3$ doped with varying amounts of Sr and La, as well as co-doped with equal quantities of Sr and La, were constructed using VESTA software, as illustrated in Fig. 7a. First-principles calculations were subsequently employed to verify the XGBoost and MLP formation energy prediction models, which demonstrated the highest goodness-of-fit in this study.

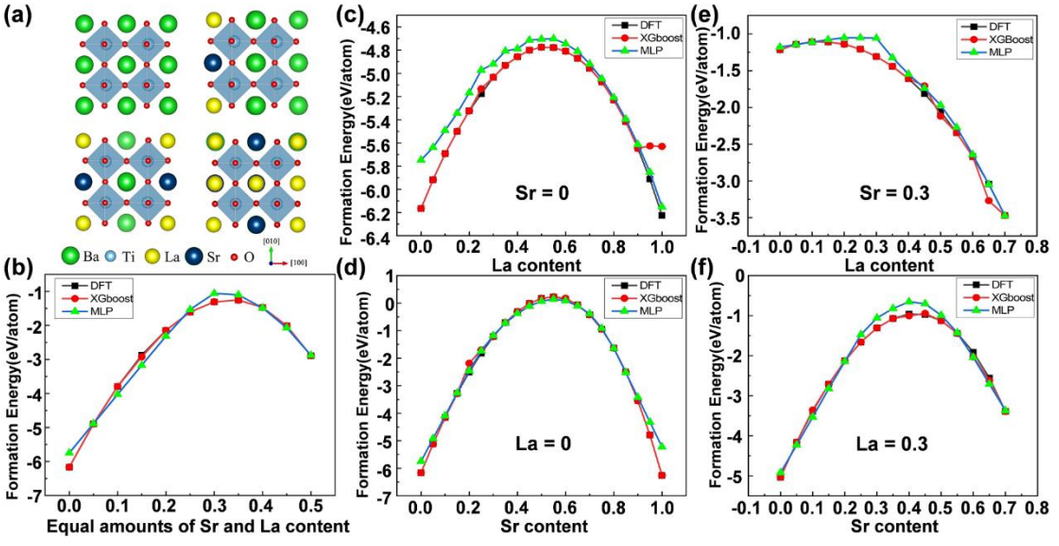

Fig. 7. (a) Lattice model of $(Ba_{1-x-y}Sr_xLa_y)TiO_3$. (b) Comparison of predicted and first-principles calculated formation energies for the Sr and La co-doped $BaTiO_3$ system with equal doping concentrations. (c-f) Comparison between predicted formation energies from models and first-principles calculated values for the Sr and La co-doped $BaTiO_3$ system.

Four cases were selected for calculation to validate the formation energy models with varying Sr and La doping levels: Sr contents of 0 and 0.3 and La contents of 0 and 0.3. The results are presented in Fig. 7 (c)-(f). As shown, when the Sr content is 0, the formation energy initially increases and then decreases with rising La content in the doped system, ranging from -6.2 to -4.7 eV, with a maximum at 0.5 La content. Conversely, when the Sr content is 0.3, the formation energy gradually decreases as La content increases, ranging from -3.5 to -1.0 eV. Comparing the predictions of the two

models at 0.3 Sr, it is evident that the XGBoost model aligns more closely with the first-principles calculations results. In both cases, as the Sr content in the doped system increases (0 and 0.3), the formation energies exhibit an overall trend of increasing and then decreasing, ranging from -6.2 to 0.5 eV and -5 to -0.5 eV, respectively, which is significantly higher than the formation energies at 0 and 0.3 for Sr content. This observation supports the earlier conclusion that Sr content markedly influences the formation energy distribution of the doped system. Overall, the formation energy distributions obtained from the XGBoost and MLP prediction models accurately reflect the actual formation energy distribution in terms of both values and trends, with the XGBoost model demonstrating superior predictive performance compared to the MLP model. For the validation of the formation energy models with equal Sr and La doping, the results are shown in Fig. 7b. The formation energy range for this doped system is approximately -6.2 to -1.0 eV, with all values being negative, indicating good thermodynamic stability. As the Sr and La co-doping levels increase, the formation energy of the doped system first rises and then decreases, peaking when the Sr and La doping levels are around 0.30 to 0.35. The formation energy distributions predicted by the XGBoost and MLP models are generally consistent with the first-principles calculations results, demonstrating the high predictive accuracy and reliability of the formation energy prediction models. Additionally, this study employs various ML models to generate comparative results for the formation energy of the doped system, which are validated through first-principles calculations (Comparison results in Table S4).

3.5 DFT-guided performance study of Sr, La co-doped $BaTiO_3$ materials

3.5.1 Ferroelectric properties

To systematically capture the influence of Sr and La co-doping on the formation energy and to enable a comparative assessment across different stability regimes, a co-doping scheme of $(Ba_{1-x-y}Sr_xLa_y)TiO_3$ with x = y = 0, 0.125, 0.25, and 0.375 was selected. This compositional range spans the main features of the formation energy profile, including the region around the maximum formation energy, thereby allowing the investigation of property variations in BT-based materials across distinct formation energy regimes. Moreover, this selection provides a representative and computationally efficient subset for subsequent first-principles calculations of the doped systems.

It should be noted that some of the higher nominal doping levels considered in this work may exceed the experimentally accessible solubility limits of La in $BaTiO_3$. These compositions are therefore treated as idealized structural models within a first-principles framework. Despite their potential thermodynamic metastability, the calculated formation energy landscape and associated property variations reliably capture the underlying doping trends and provide guidance for identifying composition ranges of interest for further experimental and theoretical investigations.

In order to elucidate the structure-property relationship between the microstructure and macroscopic performance of the $(Ba_{1-x-y}Sr_xLa_y)TiO_3$ system and deepen the understanding of ferroelectric phase transitions, this study investigated its ferroelectric properties. In the investigation of the effects of varying Sr and La co-doping levels on

the ferroelectric properties of pure $BaTiO_3$, the potential well depth (ferroelectric switching barrier) of the doped systems was first calculated. This parameter is closely related to the magnitude of ferroelectric polarization and facilitates predictions of ferroelectric phase transitions and their responses to applied electric fields. The variation trends of potential well depths obtained from first-principles calculations, Landau-Ginzburg-Devonshire (LGD) fitting parameters, macroscopic polarization (P_s), and switching barrier (E_b) under different x-doping ratios are presented in Fig. 9f. It is indicated in Table S5 that the intrinsic spontaneous polarization value of $BaTiO_3$ is 26.80 μC/cm^2, closely matching experimental values. Furthermore, a decrease in spontaneous polarization of $(Ba_{1-x-y}Sr_xLa_y)TiO_3$ with increasing x was observed, suggesting a reduction in inherent ferroelectricity; for instance, the spontaneous polarization of $(Ba_{1-x-y}Sr_xLa_y)TiO_3$ (x = y = 0.25) was measured at 19.24 μC/cm^2. The potential well depth for pure $BaTiO_3$ was determined to be 85.04 meV. Upon the introduction of Sr and La, the calculated potential well depths for $(Ba_{1-x-y}Sr_xLa_y)TiO_3$ (x = y = 0.125), $(Ba_{1-x-y}Sr_xLa_y)TiO_3$ (x = y = 0.25), and $(Ba_{1-x-y}Sr_xLa_y)TiO_3$ (x = y = 0.375) were found to be 89.63 meV, 95.08 meV, and 98.68 meV, respectively. This apparent increase in potential well depth does not directly imply enhanced macroscopic ferroelectricity. Instead, it reflects modifications in the local lattice environment induced by Sr and La substitution, which weaken cooperative Ti–O displacement and long-range dipole–dipole coupling while stabilizing localized polar distortions. Similar behavior has been reported in aliovalently co-doped $BaTiO_3$-based systems, where strong A-site chemical and charge disorder promotes relaxor-like characteristics dominated by polar nanoregions rather than classical ferroelectric domains.[44] Consequently, the increased potential well depth at high co-doping levels indicates that a greater amount of energy is required to reorient local polar units under external fields, suggesting enhanced stability of short-range polar regions rather than cooperative ferroelectric domain switching, which is consistent with the emergence of a weakly coupled or relaxor-like dielectric response.

To more intuitively visualize the ferroelectric switching barrier of $(Ba_{1-x-y}Sr_xLa_y)TiO_3$ and its temperature dependence, temperature-dependent calculations of the double-well depth and polarization intensity were subsequently performed, as shown in Fig. 8. It is evident that both the ferroelectric switching barrier and spontaneous polarization decrease with rising temperature for all compositions. Additionally, as the temperature increases, the double-well depth gradually diminishes, disappearing above approximately 600 K, indicating the thermal suppression of lattice instability. These phenomena elucidate the transition process from a polar to a paraelectric state in $BaTiO_3$-based materials and further confirm that the polarization behavior at high doping levels is intrinsically sensitive to thermal fluctuations.

Berry-phase polarization calculations were also performed to investigate the polarization behavior of the doped systems, as illustrated in Fig. 9 (a)-(d). Each point in the figure represents a transitional structural configuration along the ferroelectric-to-paraelectric pathway, with each structure corresponding to a polarized lattice state. The lines indicate the polarization branches, and the difference between the vertical coordinate of the line's midpoint and its intersection with the nearest polarization

quantum denotes the spontaneous polarization value (P_s), while the vertical spacing between adjacent lines represents the polarization quantum (P_q). The results demonstrate that the spontaneous polarization (P_s) decreases systematically with increasing doping content, indicating a gradual breakdown of long-range ferroelectric coherence and the development of weakly coupled polar behavior. For doping levels of x = y = 0, 0.125, 0.25, and 0.375, the polarization quantum values are 32.68, 34.95, 24.11, and 17.66, respectively, showing an initial increase followed by a decrease, with a maximum at x = y = 0.125. At higher doping levels, the reduced separation of polarization branches suggests that polarization primarily originates from localized ionic displacements rather than cooperative ferroelectric ordering, which is characteristic of relaxor-like systems.

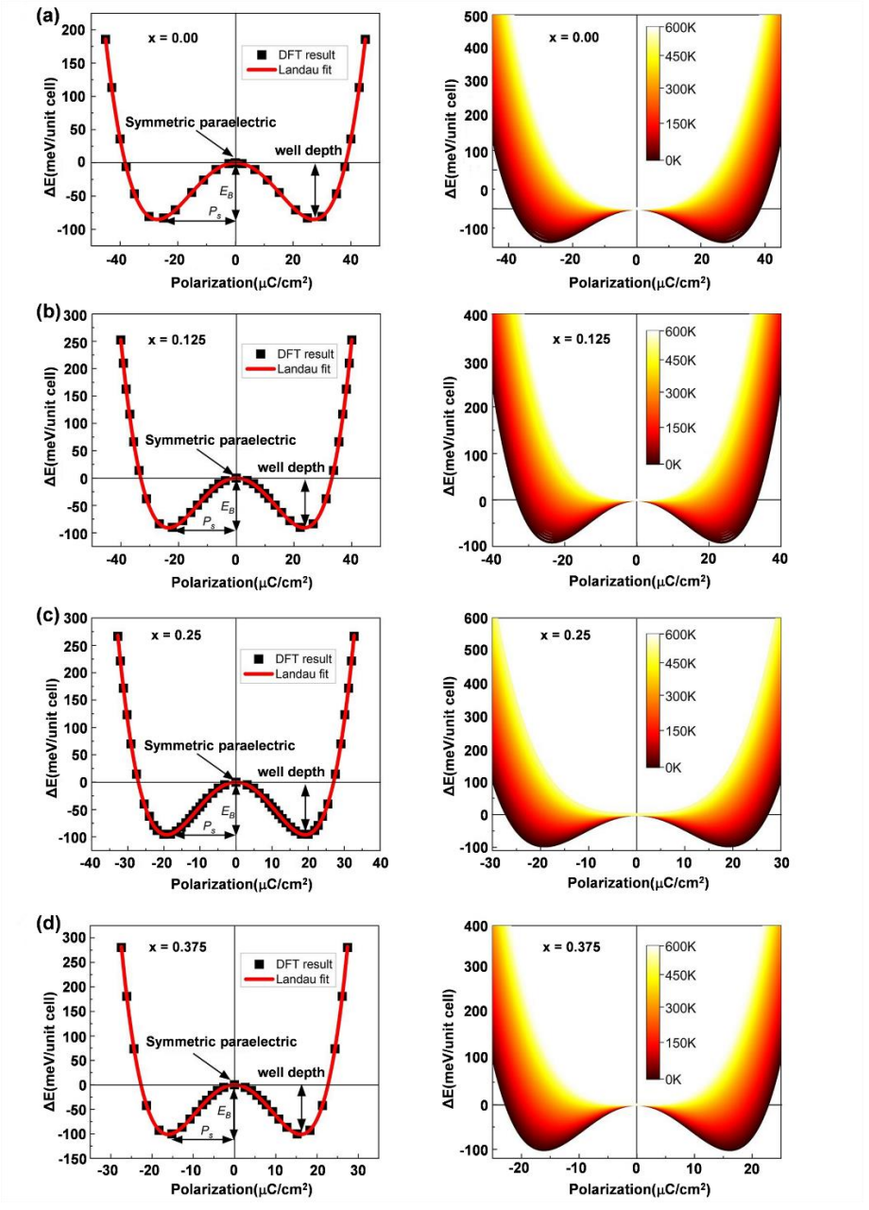

Fig. 8. Ferroelectric flip barrier and temperature dependence for $(Ba_{1-x-y}Sr_xLa_y)TiO_3$:(a) x = y = 0;(b) x = y = 0.125;(c) x = y = 0.25;(d) x = y = 0.375.

The distribution of polarization values under an applied electric field was examined, and the P–E hysteresis loops were plotted, as illustrated in Fig. 9e. Although the simulated hysteresis loops differ from those measured experimentally due to the absence of extrinsic effects such as domain-wall motion and finite-temperature kinetics, they still capture essential intrinsic trends. As indicated in Fig. 9e, with increasing doping concentration, the hysteresis loops gradually become slimmer, and both the remanent polarization (P_r) and saturation polarization (P_{max}) decrease. This behavior reflects a weakening of long-range ferroelectric switching and the emergence of a relaxor-like dielectric response characterized by reduced hysteretic loss, rather than a transition to an ideal linear dielectric. Although this study primarily investigated the effects of Sr and La co-doping on the ferroelectric properties of pure $BaTiO_3$ using first-principles calculations, prior experimental studies have consistently demonstrated that Sr and La substitution weakens macroscopic ferroelectric order and drives $BaTiO_3$-based systems from a saturated ferroelectric phase toward a weakly coupled relaxor regime.[45-48] Recent studies on aliovalently co-doped $BaTiO_3$ further indicate that high doping levels favor relaxor-like behavior associated with polar nanoregions instead of a purely linear dielectric response,[44] which is fully consistent with the trends revealed by the present first-principles simulations.

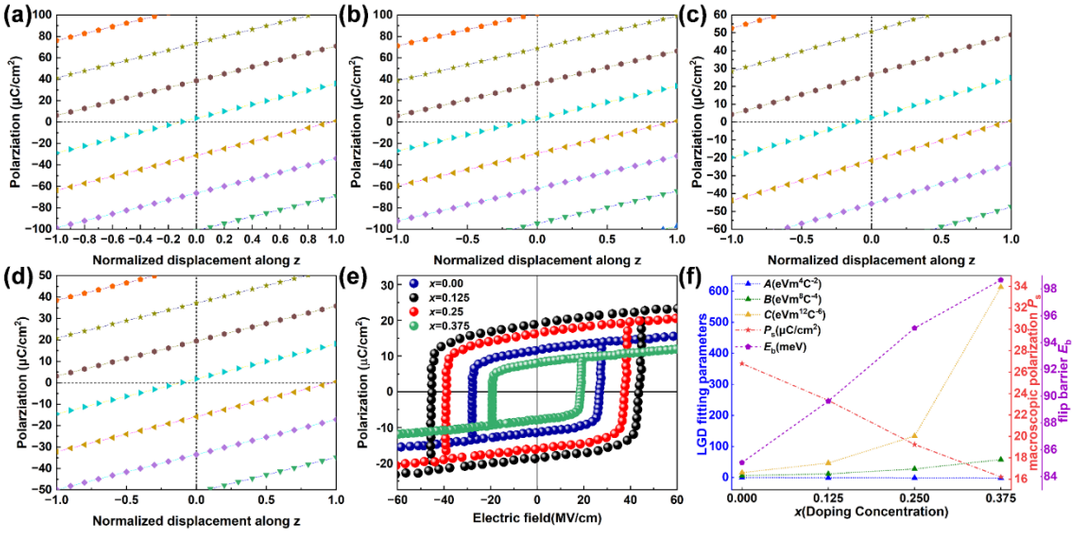

Fig. 9. (a-d) Berry phase polarization calculation diagram of $(Ba_{1-x-y}Sr_xLa_y)TiO_3$ system: (a) x = y = 0; (b) x = y = 0.125; (c) x = y = 0.25; (d) x = y = 0.375. (e) The hysteresis loops of $(Ba_{1-x-y}Sr_xLa_y)TiO_3$ system obtained by first-principles calculations. (f) Variation trends of LGD fitting parameters, macroscopic polarization P_s, and flip barrier E_b in $(Ba_{1-x-y}Sr_xLa_y)TiO_3$ under different x-doping ratios.

Overall, the calculated trends demonstrate that Sr and La co-doping drives $(Ba_{1-x-y}Sr_xLa_y)TiO_3$ from a saturated ferroelectric state toward a weakly coupled, relaxor-like dielectric regime through the progressive suppression of long-range ferroelectric coupling. In particular, the compositions in the range of x = y = 0.125–0.25 represent a characteristic crossover window, in which appreciable polarization and local polar fluctuations are retained while hysteretic loss is significantly reduced. This evolution is accompanied by enhanced dielectric linearity, improved thermal stability, and favorable

frequency response, which are highly desirable for high-frequency dielectric and energy-storage applications.[49-51] These findings align with the objective of this work to accelerate the discovery and design of capacitor materials with high-frequency response and stability.

3.5.2 Crystal structure

In order to elucidate the mechanism underlying the phase transition from the saturated ferroelectric phase to the weakly coupled relaxor phase in the $(Ba_{1-x-y}Sr_xLa_y)TiO_3$ system with increasing Sr and La co-doping concentrations, a comprehensive investigation of the crystal structures across various doping compositions was conducted. As shown in Fig. 10a, the total K-S energy decreases progressively with increasing doping concentration, suggesting an improvement in the system's structural stability. From the variations in lattice parameters and unit cell volume (Fig. 10(b) and (c)), the reduction in the lattice parameters a, c, and unit cell volume of $(Ba_{1-x-y}Sr_xLa_y)TiO_3$ can be attributed to the smaller ionic radii of Sr^{2+} and La^{3+} compared to Ba^{2+}, which causes lattice contraction. Moreover, the incorporation of La^{3+} and Sr^{2+} further reduces the difference between the lattice parameters a and c, leading to a decrease in the c/a ratio and significantly weakening the tetragonal distortion of the crystal. As illustrated in Fig. 10d, the relative ionic displacement of Ti^{4+} ions at the B site decreases with increasing doping concentration. The introduction of A-site Sr^{2+} and La^{3+} ions reduces the displacement of Ti^{4+} in the oxygen octahedra and lowers the O-Ti-O bond angle, thereby weakening the tetragonality and local dipole moment of the system. The computational results suggest that the disordered displacement of Ti^{4+} ions a primary cause of the weakly coupled relaxor behavior. Additionally, Fig. 10e shows that the incorporation of smaller Sr^{2+} and La^{3+} ions causes significant negative displacement of the Sr-O_{12} and La-O_{12} polyhedra along the [001] direction. This displacement alters the effective coordination number of the cations within these polyhedra. In the $(Ba_{1-x-y}Sr_xLa_y)TiO_3$ system, Sr and La incorporation increases the volume of Ba-O_{12} octahedra, while the volumes of Sr-O_{12} and La-O_{12} octahedra are significantly reduced compared to Ba-O_{12}. This volume change enhances the mobility of A-site ions, leading to an increased dipole moment due to the vibration or movement of the A-site ions. The influence of different A-site ions on the motion of Ti^{4+} ions further compresses the surrounding Ti-O_6 octahedra, resulting in volume changes in the Ti-O_6 octahedra in the $(Ba_{1-x-y}Sr_xLa_y)TiO_3$ structure. As shown in Fig. 10f, the volume of the Ti-O_6 octahedra in BT is 11.21 $Å^3$ and decreases gradually with increasing doping concentration. This indicates that during the compression process of the Ti-O_6 octahedra, the local angular distortion effects are gradually weakened, significantly influencing the relaxor properties and dipole distribution behavior.

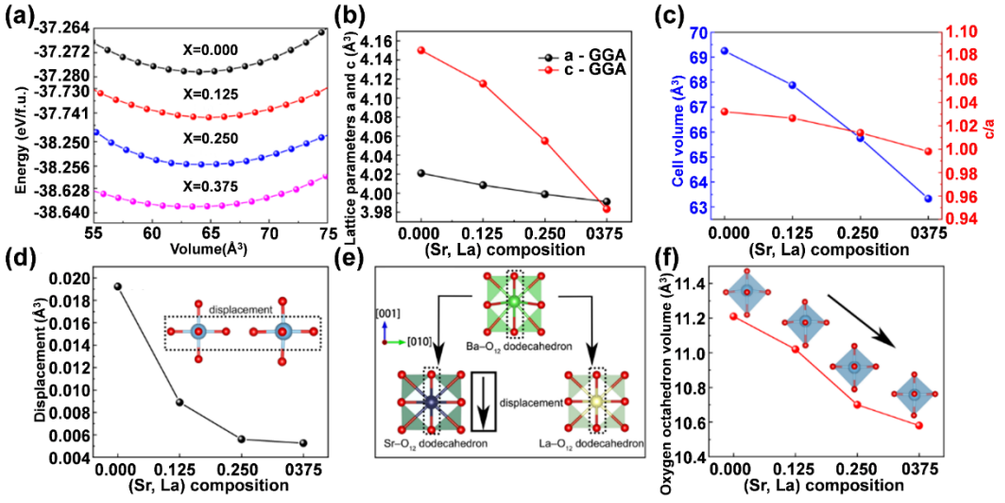

Fig. 10. (a) Variation of K-S energy with different doping compositions. (b) Changes in lattice parameters (a, c) with doping ratio. (c) Variation of unit cell volume and tetragonality ratio for different doping compositions. (d) Displacement of B-site atoms for various doping compositions. (e) A-site atomic displacement within the dodecahedron volume. (f) Changes in octahedron volume for different doping compositions.

3.5.3 Elastic anisotropy

Ensuring adequate mechanical stability during the processing and application of materials necessitated a systematic analysis of the elastic anisotropy in the $(Ba_{1-x-y}Sr_xLa_y)TiO_3$ system. Elastic anisotropy, which reflects the directional dependence of a material's elastic response, is a key parameter influencing mechanical properties and plays a critical role in optimizing device performance. First-principles calculations were used to derive the elastic stiffness matrices for various doping ratios (x = y = 0, 0.125, 0.25, 0.375), from which the bulk modulus (B), Young's modulus (Y), and shear modulus (G) were obtained. Three-dimensional distributions of these moduli were visualized to better understand their anisotropic characteristics (Fig. 11). As shown in Fig. 11a, undoped $BaTiO_3$ exhibited significant elastic anisotropy, with B displaying the most pronounced directional dependence. In contrast, Y showed weaker anisotropy, with noticeable directional extensions, while G was higher on the xoz plane compared to other planes. For the doping ratio of x = y = 0.125 (Fig. 11b), no significant change in elastic anisotropy was observed, indicating persistent strong directional dependence. As Sr and La co-doping concentrations increased (Fig. 11c and d), the elastic anisotropy gradually decreased, with a marked enhancement in isotropy. The three-dimensional modulus surfaces evolved toward spherical shapes, with B in Fig. 11d approaching a nearly perfect sphere, indicating high isotropy. While Y and G retained some directional dependencies in certain regions, their overall distributions became more uniform. These findings suggest that Sr and La doping modifies the crystal symmetry of $BaTiO_3$, significantly affecting the directional distribution of the elastic moduli. At lower doping concentrations (x = y = 0.125 and 0.25), local stress concentrations due to lattice distortions intensified the elastic anisotropy. However, at higher doping concentrations (x = y = 0.375), lattice stabilization led to a significant reduction in anisotropy. For practical high-frequency capacitor applications, a moderate degree of elastic anisotropy

is beneficial whereas excessive anisotropy promotes cracking or localized failure. First-principles calculations identify x = y = 0.25 as providing the most favorable balance of stiffness and mechanical robustness among the compositions studied.

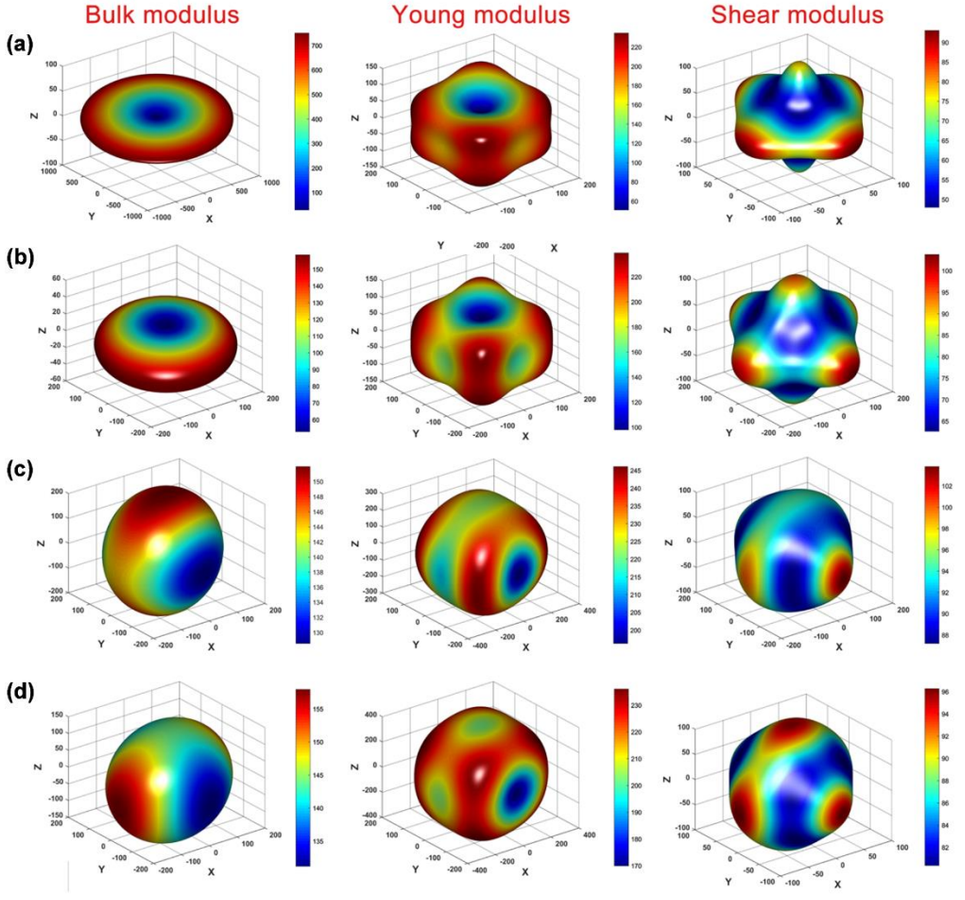

Fig. 11. Volume modulus (B), Young's modulus (Y), and shear modulus (G) of $(Ba_{1-x-y}Sr_xLa_y)TiO_3$:(a) x = y = 0;(b) x = y = 0.125;(c) x = y = 0.25;(d) x = y = 0.375.

3.5.4 Thermal properties

An appropriate operating temperature is critical for optimizing performance and extending the service life of capacitor materials. To enhance the operational stability and reliability of materials, we investigated the thermodynamic properties of $(Ba_{1-x-y}Sr_xLa_y)TiO_3$, focusing on enthalpy, entropy, Gibbs free energy, and heat capacity, aiming to optimize its thermodynamic stability within the target temperature range. This approach aims to prevent performance degradation caused by heat accumulation or phase transitions under high-frequency operating conditions. The thermodynamic parameters for different compositions were calculated as functions of temperature, as shown in Fig. 12. At low temperatures, minor differences were observed among the four compositions. However, in the high-temperature range, the composition with a doping level of x = y = 0.25 exhibited the highest entropy across the entire temperature range (Fig. 12b), indicating the greatest degree of disorder and vibrational mode diversity, which is beneficial for high-temperature thermal stability. This composition also showed the lowest Gibbs free energy (Fig. 12c), implying the highest thermodynamic stability. Although the heat capacity at x = y = 0.125 was slightly higher

than that at x = y = 0.25 (Fig. 12d), the difference was negligible, and the latter still maintained a relatively high level, suggesting that the doped material possesses strong heat absorption capability, a critical factor for efficient thermal management in high-frequency applications. Collectively, these factors contribute to the enhanced high-temperature thermal stability of BT-based materials at x = y = 0.25. Furthermore, the increase in enthalpy observed for the doped compositions in the high-temperature region suggests potential advantages for thermoelectric and phase-change material applications.

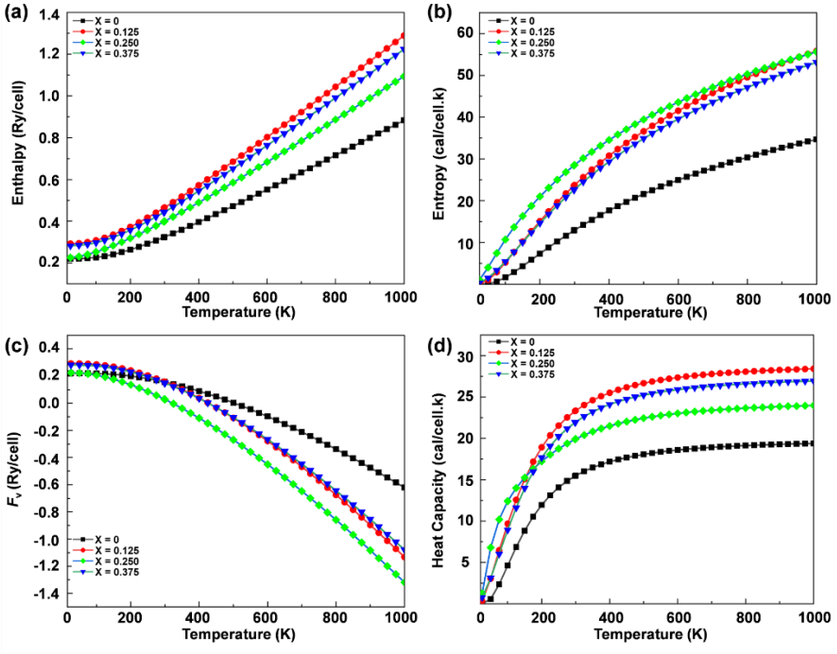

Fig. 12. Comparison of thermodynamic property parameters with temperature for $(Ba_{1-x-y}Sr_xLa_y)TiO_3$ (x = y = 0, 0.125, 0.25, 0.375): (a) Enthalpy;(b) Entropy;(c) Gibbs free energy (F_v);(d) Heat capacity.

4. Conclusions

This study employed a data-driven approach integrating machine learning with first-principles calculations to predict the formation energy of doped materials, thereby guiding material doping modifications based on the impact of doping levels on formation energy. This method accelerates the development of advanced $BaTiO_3$-based capacitor materials by rapidly screening doping compositions with weakly coupled relaxor-like dielectric characteristics and broad temperature stability. Among the six ML models used, the XGBoost model demonstrated the best performance, achieving a mean absolute error (MAE) of 0.105 eV/atom and a coefficient of determination (R^2) of 0.989 through first-principles validation. Furthermore, SHAP analysis revealed that the four most influential features on formation energy are Ba content, Sr content, A-site thermal conductivity, and A-site specific heat capacity, consistent with the preferential occupation of Sr and La at A-sites in $BaTiO_3$. This validated model enabled prediction of formation energies for 30,301 Sr, La co-doped $BaTiO_3$ configurations, identifying representative doping concentrations (0, 0.125, 0.25, and 0.375) that capture formation energy trends across extended composition spaces. Subsequent first-principles

investigations of ferroelectric properties, crystal structure, elastic anisotropy, and thermal properties at these concentrations revealed microscopic mechanisms governing the evolution of polarization behavior and relaxor-like dielectric characteristics. The results indicate that co-doping in the range of 0.125–0.25 introduces sufficient compositional and displacement disorder to progressively weaken long-range ferroelectric coupling while retaining appreciable polarization, placing the system within a representative crossover regime toward a weakly coupled, relaxor-like dielectric state. At a doping level of 0.25, the material exhibits increased vibrational entropy, reduced free energy, and higher elastic modulus, indicating enhanced thermodynamic stability, improved mechanical anisotropy, and a more uniform modulus distribution. These features are advantageous for high-temperature operational stability, stress tolerance in device packaging, and long-term capacitor reliability. Overall, this data-driven methodology provides an effective strategy for rapidly screening and designing capacitor materials with superior frequency response and stability, and offers broad potential for guiding doped-material performance optimization.

Acknowledgments

This project is partially supported by the National Natural Science Foundation of China (Grant No. 52002164, No. 52060020, No. 52162018, No. 52162019) and the Natural Science Foundation of Jiangxi Province of China (Grant No. 20242BAB25224, 20232BAB204017). The author from IMRE acknowledges supports from A*STAR, under RIE2025, IAF-ICP Grant I2301E0027. This study was partially supported by the High Performance Computing Service of the Modern Educational Technology and Information Center of Nanchang Hangkong University.

Declaration of competing interest

The authors declare that they have no known competing financial interests or personal relationships that could have appeared to influence the work reported in this paper.

CRediT authorship contribution statement

Chong Guo and Kailing Fang: writing-reviewing & editing, data curation, methodology, formal analysis, investigation, software. Haojie Yue: software, data curation, methodology, investigation. Kun Guo: conceptualization，formal analysis, funding acquisition, resources, investigation, supervision. Ziliang Deng, Zhichao Gong, Kang Li and Huacheng Zhang: data curation, formal analysis, investigation. Zhiyong Liu, Bing Xie and Pu Mao: resources, investigation. Kui Yao: investigation, resources. Chee Kiang Ivan Tan and Francis Eng Hock Tay: investigation.

Data availability

The data that support the findings of this study are available from the corresponding author upon reasonable request.

References

1 L. Chen, F. Li, B. T. Gao, C. Zhou, J. Wu, S. Q. Deng, H. Liu, H. Qi, and J. Chen, Chem. Eng. J. **452,** 9 (2023).
2 A. Jain, Y. G. Wang, and L. N. Shi, J. Alloy. Compd. **928,** 33 (2022).
3 J. J. He, C. Y. Yu, Y. X. Hou, X. P. Su, J. J. Li, C. B. Liu, D. Z. Xue, J. L. Cao, Y. J. Su, L. J. Qiao, T. Lookman, and Y. Bai, Nano Energy **97,** 10 (2022).
4 W. Zhuang, X. Zhao, Y. Y. Zhang, L. H. Zhang, and M. H. Sui, Nano Energy **126,** 9 (2024).
5 J. J. He, C. X. Wang, J. J. Li, C. Liu, D. Z. Xue, J. L. Cao, Y. J. Su, L. J. Qiao, T. Lookman, and Y. Bai, J. Adv. Ceram. **12,** 1793 (2023).
6 A. Jain, S. P. Ong, G. Hautier, W. Chen, W. D. Richards, S. Dacek, S. Cholia, D. Gunter, D. Skinner, G. Ceder, and K. A. Persson, APL Mater. **1,** 011002 (2013).
7 S. Kirklin, J. E. Saal, B. Meredig, A. Thompson, J. W. Doak, M. Aykol, S. Rühl, and C. Wolverton, npj Comput. Mater. **1,** 15010 (2015).
8 B. W. Ma, X. Wu, C. L. Zhao, C. Lin, M. Gao, B. Sa, and Z. M. Sun, npj Comput. Mater. **9,** 11 (2023).
9 J. S. Kim, J. Noh, and J. Im, npj Comput. Mater. **10,** 97 (2024).
10 J. J. He, X. P. Su, C. X. Wang, J. J. Li, Y. X. Hou, Z. H. Li, C. B. Liu, D. Z. Xue, J. L. Cao, Y. J. Su, L. J. Qiao, T. Lookman, and Y. Bai, Acta Mater. **240,** 10 (2022).
11 F. Pedregosa, G. Varoquaux, A. Gramfort, V. Michel, B. Thirion, O. Grisel, M. Blondel, P. Prettenhofer, R. Weiss, V. Dubourg, J. Vanderplas, A. Passos, D. Cournapeau, M. Brucher, M. Perrot, and E. Duchesnay, J Mach Learn Res **12,** 2825 (2011).
12 S. L. Kukreja, J. Löfberg, and M. J. Brenner, IFAC Proc. Vol. **39,** 814 (2006).
13 G. C. McDonald, WIREs Comp Stat **1,** 93 (2009).
14 S. Suthaharan, in *Machine Learning Models and Algorithms for Big Data Classification: Thinking with Examples for Effective Learning* (Springer US, Boston, MA, 2016), p. 207.
15 S.-C. Wang, in *Interdisciplinary Computing in Java Programming* (Springer US, Boston, MA, 2003), p. 81.
16 A. J. Myles, R. N. Feudale, Y. Liu, N. A. Woody, and S. D. Brown, J. Chemom. **18,** 275 (2004).
17 L. Breiman, Mach. Learn. **45,** 5 (2001).
18 T. Chen and C. Guestrin, in *Proceedings of the 22nd ACM SIGKDD International Conference on Knowledge Discovery and Data Mining* (Association for Computing Machinery, San Francisco, California, USA, 2016), p. 785.
19 Y. L. Zhu, J. S. Zhang, Z. H. Qu, S. Jiang, Y. Liu, Z. H. Wu, F. Yang, W. Hu, Z. Y. Xu, and Y. H. Dai, Ceram. Int. **50,** 6250 (2024).
20 M. Arshad, H. L. Du, M. S. Javed, A. Maqsood, I. Ashraf, S. Hussain, W. L. Ma, and H. P. Ran, Ceram. Int. **46,** 2238 (2020).
21 M. Karamzadeh-Jahromi, M. Izadifard, and M. E. Ghazi, J. Alloy. Compd. **1006,** 16 (2024).

22 S. M. Hwang, J. C. Lim, S. I. Kim, J. Y. Kim, J. Hwang, C. H. Lee, N. Kwon, I. Kim, K. Lee, S. Park, S. M. Bae, J. H. Hwang, K. Lee, and H. S. Kim, J. Eur. Ceram. Soc. **44,** 5471 (2024).
23 R. Kumar, I. Singh, R. Meena, K. Asokan, B. Birajdar, and S. Patnaik, Mater. Res. Bull. **123,** 7 (2020).
24 S. A. N. Franca, Jr., W. Acchar, S. L. A. Dantas, P. H. Chiberio, H. P. A. Alves, M. R. D. Bomio, F. V. Motta, F. Bohn, A. Ferreira, F. Vaz, and M. A. Correa, Ceram. Int. **49,** 36025 (2023).
25 R. Martínez-López, M. Pérez-Labra, J. A. Romero-Serrano, F. R. Barrientos-Hernández, M. Reyes-Pérez, M. I. Valenzuela-Carrillo, G. Urbano-Reyes, V. E. Reyes-Cruz, and G. I. Dávila-Pulido, J. Rare Earths **42,** 1920 (2024).
26 F. Zhang, J. H. Tan, P. F. Wang, R. X. Huang, H. T. Lin, X. Huang, J. Yang, Z. X. Fu, X. H. Cao, L. Zhang, S. H. Yu, and R. Sun, Ceram. Int. **50,** 38263 (2024).
27 C. A. Randall and P. Yousefian, J. Eur. Ceram. Soc. **42,** 1445 (2022).
28 S. Yan, P. Xu, G. Li, Y. Li, Y. Zhu, X. Zhu, Q. Yang, M. Li, M. Tang, H. Lu, S. Liu, Q. Li, D. W. Zhang, and Z. Chen, npj Comput. Mater. **11,** 2 (2025).
29 J. Chai, C. Ming, and Y.-Y. Sun, Appl. Phys. Lett. **123,** 252103 (2023).
30 Y. Z. Liang, M. W. Chen, Y. A. Wang, H. X. Jia, T. L. Lu, F. K. Xie, G. H. Cai, Z. G. Wang, S. Meng, and M. Liu, Sci. China-Mater. **66,** 343 (2023).
31 K. Momma and F. J. A. C. Izumi, Appl. Crystallogr. **44,** 1272 (2011).
32 G. Hua and D. J. R. A. Li, RSC Adv. **5,** 103686 (2015).
33 D. Scheiber, V. I. Razumovskiy, P. Puschnig, R. Pippan, and L. J. A. M. Romaner, Acta Mater. **88,** 180 (2015).
34 J. Hafner, J. Comput. Chem. **29,** 2044 (2008).
35 O. Diéguez, S. Tinte, A. Antons, C. Bungaro, J. B. Neaton, K. M. Rabe, and D. Vanderbilt, Phys. Rev. B **69,** 212101 (2004).
36 L. Du and H. Du, Int. J. Mod. Phys. B **30,** 1650164 (2016).
37 J. Zhang, Y. Zhang, T. Xu, and J. Wang, Phys. Rev. B **103,** 014113 (2021).
38 C. Loschen, J. Carrasco, K. M. Neyman, and F. Illas, Phys. Rev. B **75,** 035115 (2007).
39 N. V. Skorodumova, R. Ahuja, S. I. Simak, I. A. Abrikosov, B. Johansson, and B. I. Lundqvist, Phys. Rev. B **64,** 115108 (2001).
40 I. Solovyev, N. Hamada, and K. Terakura, Phys. Rev. B **53,** 7158 (1996).
41 S. Rath, G. S. Priyanga, N. Nagappan, and T. Thomas, Comput. Mater. Sci. **210,** 10 (2022).
42 S. M. Lundberg, G. Erion, H. Chen, A. DeGrave, J. M. Prutkin, B. Nair, R. Katz, J. Himmelfarb, N. Bansal, and S.-I. Lee, Nat. Mach. Intell. **2,** 56 (2020).
43 S. M. Lundberg and S.-I. Lee, Adv. Neural Inf. Process. Syst. **30,** 4765 (2017).
44 J. Chen, P. Zhao, K. Chen, F. Si, Z. Fang, S. Zhang, and B. Tang, Chem. Eng. J. **502,** 157866 (2024).
45 A. Elbasset, S. Sayouri, F. Abdi, T. Lamcharfi, and L. Mrharrab, Glass Phys. Chem. **43,** 91 (2017).
46 R. Moussi, A. Bougoffa, A. Trabelsi, E. Dhahri, M. P. F. Graça, M. A. Valente, R. Barille, and M. Rguiti, Inorg. Chem. Commun. **137,** 109225 (2022).

[47] V. S. Puli, P. Li, S. Adireddy, and D. B. Chrisey, J. Adv. Dielectr. **05,** 1550027 (2015).
[48] Y. Tian, M. Ma, Y. Chen, Z. Liu, X. Ji, H. Wu, and Q. Jing, Ceram. Int. **50,** 19571 (2024).
[49] C. Long, Z. Su, H. Song, A. Xu, L. Liu, Y. Li, K. Zheng, W. Ren, H. Wu, and X. Ding, Energy Storage Mater. **65,** 103055 (2024).
[50] A. R. Jayakrishnan, J. P. B. Silva, K. Kamakshi, D. Dastan, V. Annapureddy, M. Pereira, and K. C. Sekhar, Prog. Mater. Sci. **132,** 33 (2023).
[51] Q. Y. Zheng, B. Xie, Q. Wang, F. Xue, K. Guo, Z. Y. Liu, P. Mao, W. W. Cao, H. J. Luo, and H. B. Zhang, Chem. Eng. J. **483,** 12 (2024).